Stressing and probing with light: A thermo-optical investigation of soft solids

Rafael Gervasone, Arianna Erba, Roberto Piazza, and Stefano Buzzaccaro*
Dipartimento di Chimica, Materiali e Ingegneria Chimica "Giulio Natta," Politecnico di Milano, Piazza Leonardo da Vinci 32, 20133 Milano, Italy

(Received 27 April 2026; accepted 5 September 2026; published 30 October 2026)

Internal stresses in arrested soft solids can be generated not only by mechanical loading but also by spatially nonuniform temperature fields, which impose incompatible thermal strains and activate coupled thermoelastic and poroelastic responses. Here, we introduce an all-optical stress-and-probe protocol that combines localized near-infrared photothermal forcing with space-resolved dynamic light scattering. The setup provides (1) thermal-lensing readout of the evolving refractive-index field and (2) photon-correlation imaging of local dynamics, complemented by speckle-based velocimetry to reconstruct displacement and velocity fields. We apply the method to two contrasting soft solids. In a thermoresponsive physical gel, continuous irradiation produces a slowly strengthening lensing signal that persists after the pump is switched off; refractive-index reconstruction indicates contributions beyond purely thermo-optic effects, consistent with irreversible microstructural reorganization. Concomitantly, correlation functions reveal a long-lived modification of the relaxation dynamics, supporting a scenario where constrained thermoelastic stresses imprint residual strain and drive postexcitation stress relaxation. In an ultraweak polystyrene colloidal gel with nearly temperature-independent constitutive properties, the sample deformation is driven by a buoyancy-driven convection, whose magnitude scales with the thermal expansivity of water and increases with pump power, crossing from largely elastic recovery to partial irreversibility. Overall, this optical platform enables controlled access to ultralow, spatially distributed thermal stresses and offers a route to study stress transmission, plasticity, and cyclic photothermal fatigue in soft solids.

DOI: 10.1103/5m7y-k8kc

I. INTRODUCTION

Soft solids such as gels and glasses of colloidal or polymeric nature are archetypal arrested materials: They display slow relaxation, aging, and a strong history dependence, while supporting stresses over long times. In these systems, macroscopic rheology and yielding emerge from intermittent, spatially heterogeneous rearrangements and stress-release events occurring at the microscopic scale. Understanding how such rearrangements are triggered, correlated in space and time, and coupled to stress transmission remains a central problem in the physics of amorphous and soft glassy matter [1–3]. Most experimental access to these mechanisms relies on externally imposed mechanical loading, with geometries such as shear or compression/extension and temporal protocols, such as step strain, creep, or oscillatory loading, using rheometers or mechanical testers [4,5]. In many realistic situations, however, stresses are generated internally by distributed fields rather than by boundary motion. Temperature fields are a ubiquitous and controllable example [6]. In a solid, spatially nonuniform temperature creates incompatible thermal strains; mechanical compatibility and force balance then require local deformations that give rise to internal stresses even in the absence of external loads [7–10]. For instance, in the context of laser excitation, this thermoelastic coupling underlies the generation of elastic waves and thermoelastic stress fields by absorbed optical pulses, a problem extensively studied in metals and optical substrates [11–17]. When the material is porous and saturated by a fluid, as in rocks, soils, and colloidal gels, thermal forcing also couples to pore pressure and relative fluid/solid motion, leading to thermoporoelastic stress diffusion and transient thermal pressurization [18,19]. Hydrogels provide an especially rich soft-matter realization of these couplings: Their deformation is intrinsically linked to solvent transport, so that stresses relax over poroelastic timescales [20]. In thermoresponsive networks (e.g., poly(N-isopropylacrylamide) (PNIPAM)-like systems), temperature additionally modulates polymer-solvent affinity and the equilibrium swelling ratio, so that heating can trigger a volume phase transition under mechanical constraints [21].

Capturing this rich behavior requires probes that are simultaneously sensitive to microscopic dynamics and spatial heterogeneity. Space-resolved multispeckle techniques such as photon-correlation imaging (PCI) [22] provide exactly this capability: By combining dynamic light scattering with imaging, PCI yields time-dependent maps of dynamical activity and displacement fields in jammed and gelled soft matter [23,24]. These methods are particularly powerful under localized perturbations, where they allow one to follow how deformation, stress, and rearrangements propagate away from

*Contact author: stefano.buzzaccaro@polimi.it

Published by the American Physical Society under the terms of the Creative Commons Attribution 4.0 International license. Further distribution of this work must maintain attribution to the author(s) and the published article's title, journal citation, and DOI.

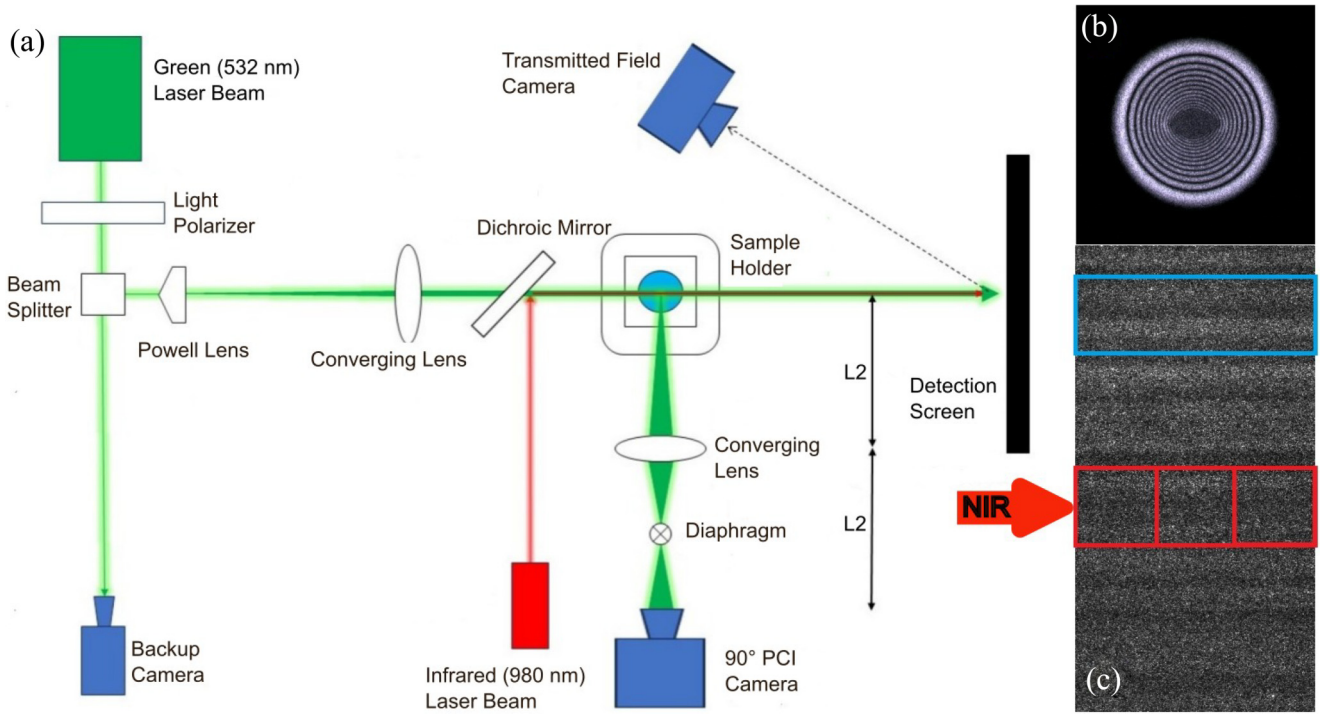


FIG. 1. (a) Schematic of the dual-wavelength pump-probe setup. The 980 nm NIR beam acts as the pump and is combined with the 532 nm probe beam by a dichroic mirror immediately upstream of the sample. The green probe is shaped into a light sheet by a Powell lens and a converging lens. A fraction of the probe beam is directed to a backup camera for monitoring. Light scattered by the sample at $\vartheta_s \simeq 90^\circ$ is collected by a stopped-down imaging system, whose diaphragm selects a narrow range of scattering wave vectors, and is recorded by the PCI camera. The transmitted NIR beam is projected onto a screen and its diffraction pattern is recorded by a dedicated transmitted-field camera, providing the thermal-lens readout. (b) Representative diffraction pattern of the transmitted NIR beam for a 9 wt% Mebiol gel. (c) Representative speckle image recorded by the PCI camera for a 9 wt% Mebiol sample. The cyan rectangle marks the unheated OR, whereas the red rectangle marks the laser-irradiated LR. The LR is further divided into three subregions; the leftmost and rightmost subregions are used for the intensity analysis discussed in the main text.

the forcing region, and how they are modulated by confinement and boundary conditions [25].

In this work, we introduce a fully optical *stress-and-probe* protocol designed to separate, within the same experiment, deformation from microscopic restructuring under thermal forcing. A focused infrared pump beam generates a localized temperature gradient and allows us to obtain a readout of the thermal field via thermal-lensing signatures, while a visible probe beam enables the reconstruction of the deformation field via image-based cross-correlation (speckle velocimetry) of speckle patterns, and the space-resolved measure of restructuring dynamics through PCI [22]. We apply this approach to two representative arrested soft solids with sharply contrasting thermomechanical couplings: a thermoresponsive physical gel (Mebiol), where temperature gradients can imprint residual stresses and trigger long-lived restructuring, and an ultraweak colloidal polystyrene gel whose intrinsic properties are approximately temperature independent and where the primary thermal effect is the possible onset of slow convection.

II. MATERIALS AND METHODS

A. Experimental setup

Figure 1 summarizes the dual-wavelength pump-probe arrangement used throughout this work. A near-infrared (NIR) beam at 980 nm acts as the pump, producing localized heating in the sample, while a 532 nm visible beam acts as the probe for space-resolved scattering measurements. The two beams are combined by a dichroic mirror immediately upstream of the sample. Two complementary detection paths are used simultaneously: The transmitted NIR field is recorded to monitor the thermal-lens (TL) response, whereas light scattered by the green probe at approximately 90° is imaged onto the PCI camera to measure local dynamics and displacements. The probe beam (Laser Quantum, Ventus 532, $\lambda = 532$ nm) was shaped into a light sheet: A Powell lens converted the initial Gaussian beam into a vertically diverging sheet, and a subsequent converging lens arrested the vertical divergence while focusing the beam in the horizontal direction. Scattered light was collected at $\vartheta_s \simeq 90^\circ$ by a stopped-down imaging system: A pinhole acted as a spatial filter, selecting the scattering wave vector $q = 23\ \mu\text{m}^{-1}$. The corresponding real-space wavelength is $2\pi/q \simeq 0.27\ \mu$m, placing the PCI measurement in the submicrometric regime and making it sensitive to local structural rearrangements of the gel. An additional low-pass IR filter was placed between the sample exit and the camera to suppress the infrared contribution. The filtered scattered light was then imaged onto a complementary metal-oxide semiconductor (CMOS) detector (Hamamatsu ORCA-flash 4.0 V2, C11440-22CU; 2048 × 2048 pixels, pixel size 6.5 × 6.5 μm). The pump source was a collimated NIR laser (JDSU S27-7602-340 module at 980 nm), yielding a beam waist

$w_0 \simeq 1.31$ mm. The pump maximum optical power was 355 mW at the collimator exit. The output power was controlled through the laser-diode driving current I_{drive} and was well described by $P(\text{mW}) = 0.625\, I_{\text{drive}}(\text{mA}) - 17.1$. The pump beam entered the sample at height of ∼6 mm from the cell bottom. The NIR transmitted beam impinged on a screen and the resulting transmitted-intensity pattern was imaged by a dedicated camera (Optika Optikam Pro 5.0). The sample holder was thermally controlled by an external thermal bath and temperature was monitored by a thermistor.

B. Photon-correlation imaging

PCI is an optical multispeckle technique that provides access to the microscopic dynamics of soft materials by measuring temporal correlations of the scattered intensity while retaining spatial resolution within the scattering volume [22,26,27]. In contrast to standard point-detection dynamic light scattering, PCI records on a multipixel sensor a *speckled* image of the illuminated region: Each pixel (or group of pixels) collects the interference of fields scattered by a finite portion of the sample, so that time correlations can be computed in parallel over many independent speckles, enabling rapid ensemble averaging and the possibility to probe dynamical heterogeneity by selecting distinct regions of interest (ROI). In our PCI setup, the measurement is performed at a fixed scattering angle ϑ_s, corresponding to a scattering wave vector

$$q = \frac{4\pi n}{\lambda} \sin\left(\frac{\vartheta_s}{2}\right), \tag{1}$$

where n is the sample refractive index and λ is the vacuum wavelength of the probe beam. Selection of a narrow range of q is achieved by imaging the scattering volume through an optical system whose numerical aperture is reduced by a diaphragm placed in the focal plane of the collection lens ("stopped-down" imaging). This Fourier-plane aperture simultaneously (1) fixes the collected scattering angle (hence q) and (2) promotes the formation of a high-contrast speckle pattern on the detector. As in conventional light-scattering correlation spectroscopy, the fundamental observable is the normalized intensity autocorrelation function

$$g_2(\tau) = \frac{\langle I(t_0)\, I(t_0+\tau)\rangle_T}{\langle I(t_0)\rangle_T^2}, \tag{2}$$

where $\langle\cdot\rangle_T$ denotes a time average over a measurement duration T. When the dynamics is not stationary (e.g., during gelation or structural evolution), T must be chosen short compared to the timescale over which the average intensity changes, so that g_2 remains meaningful at a given t_0. If the scattered field obeys Gaussian statistics, the intensity and field correlation functions are related through the Siegert relation, $g_2(\tau) - 1 = B|g_1(\tau)|^2$, where $B \leqslant 1$ is the experimental coherence (speckle-contrast) factor, which depends on the detection optics and on the ratio between the speckle and pixel sizes.

In PCI, correlations are conveniently computed by comparing two camera frames separated by a delay τ. By averaging over a set of pixels belonging to a given ROI, we define the two-time normalized correlation index

$$c_I(\tau; t_0) = \frac{\langle I(\mathbf{x}, t_0) I(\mathbf{x}, t_0+\tau)\rangle_{\text{ROI}}}{\langle I(\mathbf{x}, t_0)\rangle_{\text{ROI}} \langle I(\mathbf{x}, t_0+\tau)\rangle_{\text{ROI}}} - 1, \tag{3}$$

where $\langle\cdot\rangle_{\text{ROI}}$ indicates a spatial average over pixels in the ROI. In general, $c_I(\tau; t_0)$ depends on t_0 when the sample is aging or evolving. To reduce statistical noise while preserving temporal resolution, $c_I(\tau; t_0)$ is further averaged over a short-time window δt_0, with δt_0 much smaller than the evolution timescale.

In our analysis, the field correlation function is normalized using the zero-delay value of the intensity correlation. Since $\langle c_I(0; t_0)\rangle_{\delta t_0} = B$, the experimental contrast factor cancels, and

$$g_1(\tau) = \left[\frac{\langle c_I(\tau; t_0)\rangle_{\delta t_0}}{\langle c_I(0; t_0)\rangle_{\delta t_0}}\right]^{1/2}. \tag{4}$$

Thus, all the field correlation functions reported below are normalized to $g_1(0) = 1$, independently of the experimental speckle contrast.

Because PCI is based on imaging, it allows one to compute correlation functions locally by tiling the speckle image into multiple ROIs and comparing their $g_2(\tau)$, thus revealing spatial heterogeneity in the microscopic dynamics when present. Mesoscopic displacement and velocity fields were obtained by speckle velocimetry, based on the spatial cross-correlation of speckle images acquired at different times.

C. Thermal lensing

The transmission of a coherent laser beam through a weakly absorbing soft material can produce a spatially varying refractive index that acts as an effective TL [28,29]. While in simple fluids, the TL effect is only due to thermal expansion, the physical mechanism that creates an intensity-dependent refractive index in multicomponent systems can have different origins such as change of sample composition and thermodiffusion effects [30–32]. The refractive index can be written as

$$n(\mathbf{r}, t) = n_0 + \Delta n(\mathbf{r}, t), \tag{5}$$

where n_0 is the refractive index of the unperturbed medium and $\Delta n(\mathbf{r}, t)$ indicates the refractive-index change due to the laser absorption. The additional optical phase accumulated across a sample of thickness L is

$$\Delta\phi(x, y, t) = \frac{2\pi}{\lambda} \int_0^L \Delta n(x, y, z, t)\, dz, \tag{6}$$

with λ the vacuum wavelength and z the laser propagation direction. Introducing the path-averaged refractive-index variation

$$\overline{\Delta n}(x, y, t) = \frac{1}{L} \int_0^L \Delta n(x, y, z, t)\, dz. \tag{7}$$

Equation (6) can be written as

$$\Delta\phi(x, y, t) = \frac{2\pi}{\lambda} L\, \overline{\Delta n}(x, y, t). \tag{8}$$

The exit-plane field can then be modeled as the incident Gaussian envelope multiplied by a phase factor

$\exp[-i\Delta\phi(x,y,t)]$, and the transmitted-intensity distribution is obtained by paraxial propagation. For radially symmetric phase profiles $\Delta\phi(r,t)$, the far-field intensity can be written as a Hankel transform,

$$I(\theta,t) = I_0\left|\int_0^\infty \exp\left[-\frac{r^2}{w^2} - i\Delta\phi(r,t)\right]J_0(kr\theta)\,r\,dr\right|^2, \tag{9}$$

where w is the beam waist at the sample, $k = 2\pi/\lambda$, θ is the diffraction angle, and J_0 is the Bessel function of order zero.

In the case of simple liquid samples, absorption-induced heating generates a temperature field $\Delta T(\mathbf{r},t)$ that is transported not only by diffusion but also by buoyancy-driven flow [33]. Accordingly, the temperature dynamics is described by an advection-diffusion equation,

$$\frac{\partial \Delta T}{\partial t} + \mathbf{v}(\mathbf{r},t)\cdot\nabla\Delta T = D_{\rm th}\nabla^2\Delta T + S(\mathbf{r}), \tag{10}$$

where $D_{\rm th}$ is the thermal diffusivity, $\mathbf{v}$ is the convective velocity field, and $S(\mathbf{r})$ represents the volumetric heat source proportional to the absorbed optical power. In this regime, the refractive-index change is predominantly thermo-optic,

$$\Delta n(\mathbf{r},t) \simeq \left(\frac{dn}{dT}\right)\Delta T(\mathbf{r},t), \tag{11}$$

but the presence of $\mathbf{v}(\mathbf{r},t)$ in Eq. (10) generally breaks radial symmetry. As a consequence, the recorded interference pattern is not strictly circular, and Eq. (9) is no longer applicable in its radially reduced form. Studies of thermal-lens transients are not restricted to liquids: Time-resolved TL has been formulated and exploited as a broadband thermoelastic spectroscopy to access relaxing thermal expansivity and specific heat in supercooled glass formers [34]. More generally, TL is a well-established photothermal diagnostic in solid materials (e.g., optical glasses and polymers) to quantify thermo-optic and thermal-transport parameters [35,36]. In the case of many arrested systems, such as the Mebiol gels we studied in this work, macroscopic flow is strongly suppressed and convection is negligible. The optical response is therefore well approximated as radially symmetric, yielding circular interference fringes compatible with Eq. (9). In multicomponent gels, however, the refractive-index modulation may contain contributions in addition to the direct thermo-optic response. For the Mebiol gel investigated here, we therefore write

$$\overline{\Delta n}(r,t) = \left(\frac{dn}{dT}\right)\overline{\Delta T}(r,t) + \overline{\Delta n}_{\rm nt}(r,t), \tag{12}$$

where $\overline{\Delta n}_{\rm nt}$ denotes a contribution beyond the direct thermo-optic response (e.g., concentration/phase rearrangement, local network reorganization, or other thermally activated but not purely thermo-optic mechanisms). We can model the gel response through an effective radial phase profile

$$\Delta\phi(r,t) = \frac{2\pi}{\lambda}L\left[\left(\frac{dn}{dT}\right)\overline{\Delta T}(r,t) + \overline{\Delta n}_{\rm nt}(r,t)\right]. \tag{13}$$

Equation (9) provides the forward relation between an assumed radial phase profile and the measured diffraction pattern. In principle, a quantitative phase profile could therefore be obtained by fitting the complete diffraction pattern. In the present experiment, however, such an inversion would require a specific parametrization of the slowly evolving structural contribution and an independently known spatial temperature profile. Moreover, the transmitted-beam images were acquired with the exposure optimized to follow the outermost diffraction ring rather than for quantitative phase retrieval over the full dynamic range. We therefore do not attempt to extract an absolute $\Delta n_{\rm nt}(r,t)$ from the ring patterns. Nevertheless, the evolution of the outermost ring provides a useful semiquantitative measure of the increase in lens strength. As discussed in the Appendix, under a fixed-shape approximation for the phase profile, the outer-ring radius is approximately proportional to the amplitude of the phase modulation in the strong-lensing regime.

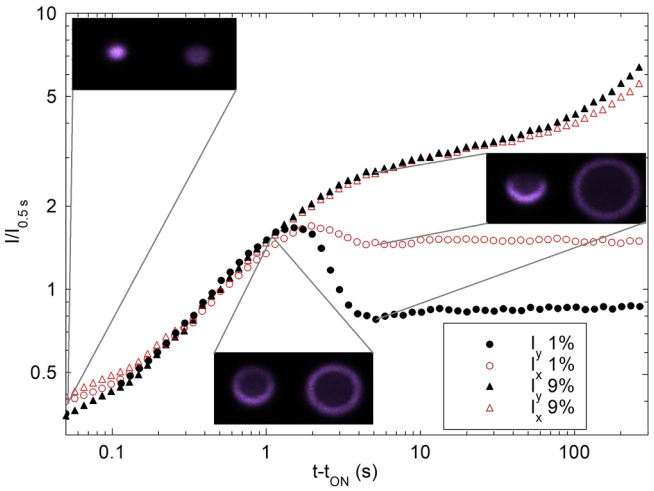


FIG. 2. Time evolution of the inertia moments I_x and I_y, normalized to their respective values at $t - t_{\rm ON} = 0.5$ s of the transmitted-field diffraction pattern for Mebiol samples at $T = 30\,^\circ$C, at 1% (liquid) and 9% (gel) polymer concentration (symbols as in the legend). Insets show representative transmitted-beam diffraction images (left: 1%; right: 9%) acquired at $t - t_{\rm ON} = 0$ (immediately after switching on the NIR beam), at $t - t_{\rm ON} = 1.5$ s (onset of symmetry breaking in the liquid pattern due to convection), and at $t - t_{\rm ON} = 5$ s (steady-state thermal profile; the diffraction pattern from the liquid sample subsequently remains unchanged). Camera exposure was optimized to track the temporal evolution of the outermost diffraction ring; consequently, the inner rings are less visible than in Fig. 1(b).

As shown in panel (b) of Fig. 1 and in the snapshots of Fig. 2, in the absence of appreciable convection the transmitted-intensity pattern is approximately radially symmetric and consists of a series of concentric rings, as observed for the Mebiol gel. In the liquid Mebiol sample, instead, buoyancy-driven convection develops along the vertical direction, parallel to gravity, and progressively breaks the radial symmetry of the pattern. To quantify both the overall expansion of the diffraction pattern and its possible symmetry breaking, we introduce simple statistical quantities that can be computed from the collected images. Let $I(x,y) \geqslant 0$ denote the image intensity at pixel coordinates (x,y). We can define: *Total mass (zeroth moment).*

$$M = \sum_{i,j} I_{ij}.$$

First moments (center of mass).

$$\bar{x} = \frac{1}{M}\sum_{i,j} x_i I_{ij}, \quad \bar{y} = \frac{1}{M}\sum_{i,j} y_j I_{ij}.$$

Second moments (moments of inertia). Interpreting intensity as mass density, the (area) moments of inertia of the distribution about axes through the centroid are

$$I_x = \sum_{i,j}(x_i - \bar{x})^2 I_{ij}, \quad I_y = \sum_{i,j}(y_j - \bar{y})^2 I_{ij}.$$

D. Materials

1. Mebiol

Mebiol® (Cosmo Bio Co., Ltd., Tokyo, Japan) is a thermoresponsive polyethylene glycol (PEG)-based polymer obtained by coupling suitably activated N-isopropylacrylamide-co-n-butyl methacrylate (NIPAAm-co-BMA) segments with diamino-PEG6000 (corresponding to 230 ethylene glycol repeat units). Although the exact composition is patented and unknown, the material is generally described as containing an overall PEG6000 fraction of approximately 34 wt% and a random, broadly polydisperse distribution of poly(NIPAAm-co-BMA) thermosensitive blocks, with a BMA molar fraction of about 5%, a key parameter in tuning the sol-gel transition temperature. The phase behavior, microscopic dynamics, and rheological properties of Mebiol have been reported elsewhere, to which the reader is referred for additional details on sample characteristics [26,27].

The polymer was provided as a sterile lyophilized powder in a sealed flask. A concentrated stock solution was prepared by adding 50 ml of sterile aqueous medium to 5 g of polymer and keeping the flask refrigerated at 4 °C, with occasional gentle shaking until a homogeneous solution was obtained. The stock was then stored in the refrigerator for several days to ensure complete hydration/dissolution and to allow entrapped air bubbles generated during reconstitution to dissipate. This mother batch, at a nominal concentration of 9%, was used as is or was subsequently diluted with distilled water to obtain a concentration of 1%. The Mebiol samples were loaded into optical cells with an optical path length $L = 5$ mm along the NIR-beam propagation direction.

2. Polystyrene gel

We studied a suspension of monodisperse polystyrene (PS) latex spheres (diameter 51 nm, refractive index $n = 1.59$, Polybead® Microspheres) dispersed at a low volume fraction ($\phi \approx 3 \times 10^{-4}$), a condition chosen to minimize multiple-scattering contributions. The particles were dispersed in an H_2O/D_2O mixture whose composition was tuned to match the particle density, thereby suppressing sedimentation. Aggregation was triggered by adding $CaCl_2$ to a final concentration of 16 mM. The suspension was then promptly transferred into an optical cuvette (cross section 2×10 mm) and filled to a height of $\simeq$10 mm. Since the used $CaCl_2$ concentration lies only slightly above the critical flocculation threshold, the aggregation kinetics are quite slow: We let the sample rest unperturbed for 72 h at a controlled temperature (typically 20 °C) before illuminating it with the IR laser.

III. RESULTS

A. Mebiol: a thermoresponsive gel

1. Thermal lens

In this section, we compare the TL response of two Mebiol samples with different compositions. The diluted sample ($c =$ 10 g/l) behaves as a liquid, whereas the concentrated sample ($c = 90$ g/l) is in the gel state. All measurements were performed at $T = 30$ °C.

Figure 2 reports the time evolution of the far-field diffraction pattern in the two cases. We begin with a qualitative description of the images. At early times, the transmitted beam has a Gaussian profile for both samples. Shortly after illumination, a circular ring pattern appears; however, after approximately 1 s the two samples exhibit markedly different behaviors. For the liquid sample, the ring expansion rapidly slows down and a pronounced vertical asymmetry develops, consistent with the onset of buoyancy-driven convection. After about 5 s, the pattern reaches a steady state. In contrast, in the gel sample the diffraction pattern remains radially symmetric and continues to expand.

The main panel of Fig. 2 shows the temporal evolution of the moments of inertia I_x and I_y, normalized by their values at $t = 0.5$ s. This reference time was chosen to avoid possible transients associated with the NIR-laser switch on. For $t \leqslant 1$ s, the liquid and gel samples follow essentially the same dynamics, indicating that the TL response is initially governed by the formation of the temperature profile. At short times, thermal diffusion dominates. Using the pump-beam radius $w_0 = 1.31$ mm and $D_{\rm th} = 1.4 \times 10^{-1}$ mm^2 s^{-1}, the thermal diffusivity of water near 30 °C [37], which provides a reasonable approximation for the highly hydrated Mebiol sample, the characteristic diffusion time is

$$\tau_{\rm th} = \frac{w_0^2}{4D_{\rm th}} \simeq 3 \text{ s}. \tag{14}$$

Consistently, for the gel sample—where convection is negligible—the growth of the diffraction ring clearly slows down for $t \gtrsim 3$ s.

For the liquid sample, I_x increases with time and eventually saturates, whereas along the vertical axis I_y first rises to a maximum and then decreases, reaching at long times a value smaller than that measured horizontally. This behavior can be understood in terms of optothermal self-lensing in a convecting liquid. As the beam propagates through the medium, a fraction of the optical power is absorbed, producing a temperature increase and—through the thermo-optic coefficient—a reduction of the refractive index. Because the intensity profile is Gaussian, the index change is largest on axis, so the sample acts as an aberrated diverging lens and generates a ring-shaped diffraction pattern. Once buoyancy-driven flow develops, the upward motion partially smooths the temperature field in the upper portion of the heated region, thereby reducing the local refractive-index gradient and the associated phase modulation. The diffraction angle is therefore smaller in the upper region, and the interference pattern progressively appears vertically compressed. The gel sample, in contrast, displays an anomalous long-time response. While the overall size of the interference pattern changes only weakly for 3 s $\leqslant t \leqslant$ 30 s, beyond $t \approx 30$ s both I_x and I_y start to grow more rapidly

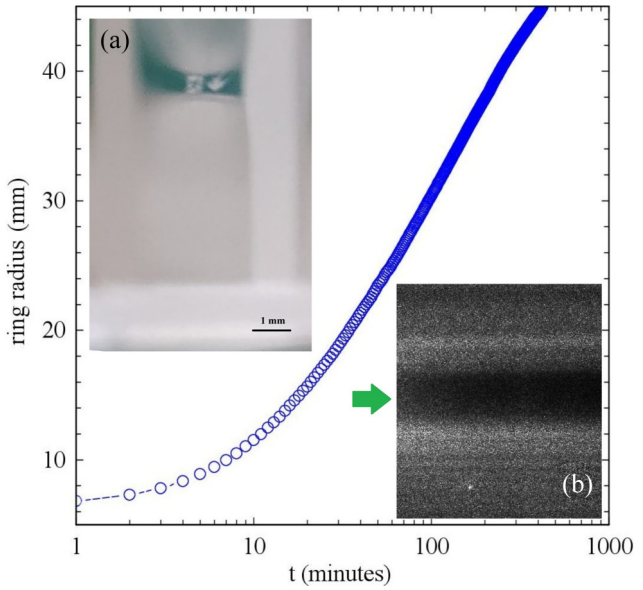


FIG. 3. Long-time evolution of the radius of the outermost diffraction ring for a 9% Mebiol sample under continuous NIR irradiation. (a) Photograph of the laboratory emergency-exit sign imaged through the thermal lens formed in the sample after 10 h of NIR illumination. Inset (b) shows the speckle field recorded by the PCI camera after one day of NIR irradiation. The arrow indicates the propagation direction of the green probe beam, as in Fig. 1. The strong diverging lens induced by the NIR heating deflects the probe beam away from its original propagation direction, so that little scattered light is detected from the region immediately downstream of the lens, which therefore appears as a dark band.

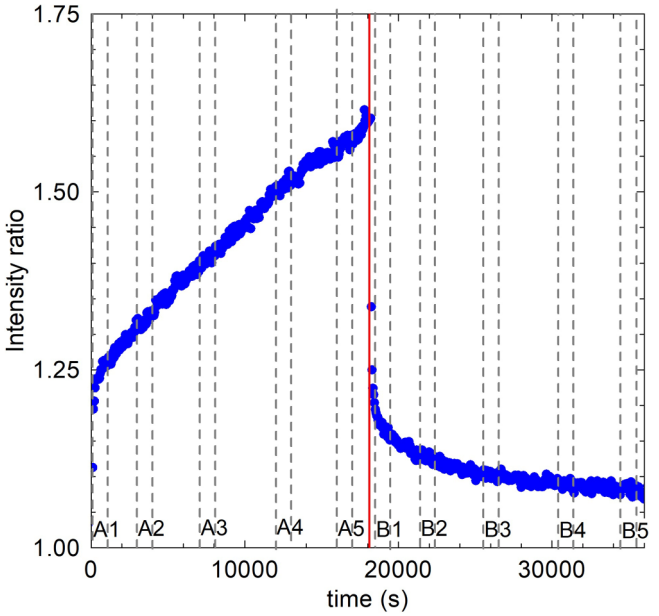


FIG. 4. Time evolution, for a 9 wt% Mebiol gel, of the ratio between the scattered-light intensity measured in the initial and final portions of the laser region LR [first and third subregions of the red rectangle in Fig. 1(c)]. The vertical red line marks the time at which the NIR laser was switched off. Time windows A1–A5 (NIR on) and B1–B5 (NIR off) indicate the intervals at which the PCI analysis reported in Fig. 5 was performed.

and in a similar fashion. This indicates the emergence of an additional mechanism that locally modifies the refractive index beyond a purely thermal contribution. Figure 3 follows, over 6 h, the time evolution of the radius of the outermost ring produced by illuminating the gel sample. The lensing effect becomes progressively stronger with no evidence of saturation; at long times, the ring radius increases approximately logarithmically. After one day, the induced diverging lens is strong enough to deflect the green probe beam almost completely, as illustrated in inset (b), where the region downstream of the lens appears dark.

Remarkably, the lensing does not vanish after switching off the infrared illumination. The induced deformation is persistent, pointing to an irreversible restructuring of the gel in the region exposed to the infrared beam. This permanent lens effect is illustrated in panel (a): The sample was removed from the holder and used as a *lens* to image the emergency-exit sign in our laboratory. A complementary reconstruction of the long-time refractive-index profile from the residual illumination stripes is presented in the Appendix. We now turn to the PCI analysis to investigate the concomitant microscopic dynamics and mechanical response of the gel.

2. PCI analysis: the role of the thermoelastic stress

In the following, we compare two regions within the gel sample, highlighted in panel (c) of Fig. 1 by a cyan rectangle (outside region, OR) and a red rectangle (laser region, LR). The OR is located far from the volume illuminated by the IR beam, whereas the LR corresponds to the portion of sample directly heated by the IR radiation.

We first consider the evolution of the scattered-light intensity. Upon switching on the IR laser, the scattered intensity from the OR remains essentially unchanged. In contrast, the intensity measured in the LR increases rapidly. Previous measurements on the same 9 wt% Mebiol system under spatially uniform heating showed a strong, approximately exponential dependence of the stationary scattered intensity on temperature, with a logarithmic slope of about 0.11 K^{-1} in the temperature range relevant here. This provides a semiquantitative estimate of the temperature scale associated with the initial intensity increase, which is consistent with a local temperature rise of approximately $\Delta T \simeq 3\ ^{\circ}C$.

We stress that the value $\Delta T \simeq 3\ ^{\circ}C$ should be regarded as an estimate rather than as a precise intensity-to-temperature calibration. In the reference measurements, the scattered intensity was recorded after allowing the sample to equilibrate at each temperature for at least 15 min, whereas here the thermal contribution must be estimated from the initial response over a few seconds, before the slower structural evolution becomes substantial.

Moreover, the intensity within the LR is spatially nonuniform: It is higher near the side where the IR beam enters the sample than near the exit side. A plausible explanation is the attenuation of the IR beam along its propagation direction, resulting in a larger optical power density, and hence a slightly larger temperature increase, in the upstream portion of the LR.

Figure 4 shows the ratio between the scattered intensities measured in the two regions. Prior to IR illumination, the

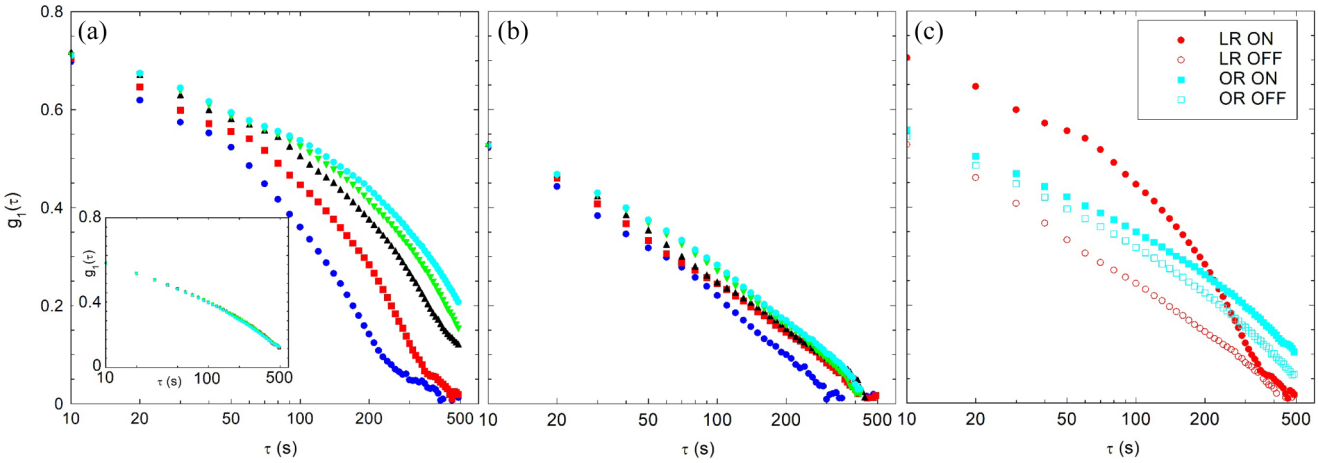


FIG. 5. (a) Field correlation functions $g_1(\tau)$ measured in a 9 wt% Mebiol gel in the laser region LR during NIR irradiation for the five time windows defined in Fig. 4: A1 (blue circles), A2 (red squares), A3 (black up triangles), A4 (green down triangles), and A5 (cyan circles). Inset: $g_1(\tau)$ measured in the OR over the same time windows (same color code as in the main panel), showing an excellent collapse within experimental uncertainty. (b) Field correlation functions measured in LR after switching the NIR laser off, for the five time windows B1–B5 defined in Fig. 4 [symbols and colors as in panel (a)]. (c) Comparison of $g_1(\tau)$ measured in LR and OR in the time windows A3 (laser on) and B3 (laser off); symbols are defined in the legend.

intensities are comparable and the ratio is close to unity. Immediately after turning on the IR beam, the ratio rises within a few seconds to approximately 1.25, a timescale consistent with the establishment of the temperature profile in the illuminated region. Surprisingly, the ratio then continues to increase approximately linearly for about 18 000 s. Such a long-term drift cannot be explained by thermal effects alone. As already suggested by the thermal-lens measurements, an additional slow mechanism becomes relevant at longer times and modifies the local concentration and/or refractive index of the sample.

After 18 500 s, the IR laser is switched off. The temperature relaxes quickly and the intensity ratio decreases accordingly. However, the ratio does not return to a value close to unity, as would be expected for a fully reversible perturbation. Over the following 18 000 s, the ratio continues to decrease slowly, indicating a gradual homogenization, but it never recovers its initial level. This provides further evidence that the IR exposure induces a persistent restructuring of the gel in the illuminated region.

To further clarify this behavior, we performed a time-resolved PCI analysis. The full time series was partitioned into ten time windows: five acquired while the IR laser was on (labeled by A1–A5) and five acquired after the IR beam was switched off (labeled by B1–B5). For each window, we computed the intensity correlation function by averaging over a 1000 s interval. For reference, the same analysis was carried out at the same time windows for the OR region.

In the OR region, the microscopic dynamics remains essentially unperturbed and shows no significant temporal evolution [see inset of Fig. 5(a)]: All the field correlation functions superimpose. The situation is markedly different in the LR [see main panel of Fig. 5(a)]. Immediately after turning on the IR beam, the correlation at the shortest plotted delay, $\tau = 10$ s, increases from $\simeq$0.55 before illumination, a value comparable to that measured in the OR, to $\simeq$0.70. Since all curves are normalized to $g_1(0) = 1$, this increase indicates a reduced decorrelation over the first 10 s and hence a slowing down of the local dynamics. As the IR exposure proceeds, the dynamics progressively slows down. In the A1 interval, the correlation function decays to zero within approximately 300 s, whereas after 16 500 s of irradiation (A5) the correlation remains significantly above zero even at $\tau = 500$ s.

After switching off the IR laser, the LR correlation function changes rapidly and the dynamics speeds up [see Fig. 5(b)]. In the first postirradiation interval (B1), the value of $g_1(\tau)$ at the shortest plotted delay, $\tau = 10$ s, returns to about 0.55, consistent with the unperturbed case, and the system decorrelates again on a timescale of order 300 s. At later times, the dynamics slows down (aging), but the effect is substantially weaker than during the irradiation stage.

The impact of the localized perturbation induced by the IR beam becomes clearer by comparing the correlation functions measured in the LR and OR at $t \approx 3500$ s after the onset of irradiation. Figure 5(c) shows that, at short delay times, the dynamics in the LR is slower than in the OR. This is not unexpected: The temperature in the LR is higher by a few degrees and, under homogeneous conditions, the microscopic dynamics of Mebiol is known to slow down upon increasing temperature [27]. At longer delays, however, the trend reverses. For $\tau \gtrsim 200$ s, $g_1(\tau)$ in the LR falls below the corresponding curve in the OR. In particular, at $\tau = 500$ s the LR signal is fully decorrelated, whereas the OR still retains a finite correlation, indicating slower relaxation far from the irradiated region.

An even more intriguing behavior emerges when we compare the LR and OR correlation functions measured about 3500 s after the IR laser has been switched off. At this stage, the two regions are essentially at the same temperature and one would therefore expect comparable dynamics. Indeed, at short delays ($\tau \lesssim 10$ s) the two curves nearly coincide. At longer delays, however, the LR decorrelates faster than the OR, i.e., the previously irradiated region relaxes more rapidly than the unperturbed one.

Importantly, this behavior is not observed in control experiments in which a Mebiol sample is heated uniformly to a higher temperature and subsequently cooled back to a lower temperature: In that case, the dynamics at lower temperature remains slower than at higher temperature, with no inversion at long delays. The anomalous relaxation measured here is therefore a consequence of the *spatial* temperature gradient (and the associated stress field) generated by local IR irradiation. We also considered whether the long-lived response could originate from ordinary aging or from effects specific to the NIR irradiation rather than from the localized thermomechanical perturbation. The OR provides a simultaneous internal aging control: It belongs to the same sample and is monitored over the same experimental time windows, yet its correlation functions remain essentially unchanged within experimental uncertainty (see the inset of Fig. 5). Together with the uniform-heating control described above, this indicates that spontaneous aging alone cannot account for the markedly different evolution observed in the LR, although some contribution from the intrinsic aging of the physical gel cannot be strictly excluded. A direct photochemical origin also appears unlikely. The pump wavelength (980 nm) lies in the near-infrared absorption band exploited for photothermal heating of water, and no absorbing chromophore is added to the sample. The excitation is therefore expected to act predominantly through heating rather than direct photochemistry. Mebiol is also reported to form a transparent thermoreversible gel without macroscopic syneresis. We cannot, however, exclude a local redistribution of solvent and polymer induced by the temperature gradient and the associated stress field; such a process is included here among the slow structural contributions to the refractive-index response. A plausible mechanism is that the mechanical and rheological properties of Mebiol depend sensitively not only on temperature but also on the presence of local T gradients. In the absence of thermal expansion, a spatial gradient in elastic stiffness alone does not generate spontaneous deformation: The undeformed configuration remains kinematically compatible with rigid platens, and no internal stress is required to satisfy equilibrium. The picture changes when the material exhibits a thermal expansion that depends on T. Then, different regions would undergo different free thermal strains under the imposed temperature gradient, but the global constraint prevents any net change in length, forcing the development of a self-equilibrated internal stress state [38]. In gels, the mechanical response is additionally controlled by solvent permeation, giving rise to poroelastic relaxation timescales and spatially inhomogeneous stress diffusion [20]. Moreover, in thermoresponsive networks, temperature strongly modulates both equilibrium swelling and mechanical properties, which amplifies stress gradients and heterogeneity under ∇T [21]. In Mebiol, because the elastic modulus increases with temperature, the colder (more compliant) portion accommodates a larger share of the mechanically induced strain needed to enforce the constraint, whereas the hotter (stiffer) region deforms less. The outcome is a nonuniform strain distribution under an overall constrained thermoelastic response, consistent with classical linear thermoelasticity for heterogeneous media and standard treatments of thermal stresses under kinematic constraints [7,39]. An order-of-magnitude estimate confirms that

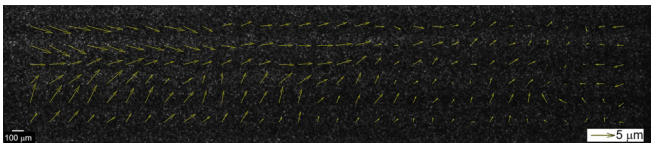


FIG. 6. Cumulative displacement field measured in a 9 wt% Mebiol gel in the laser region LR over the first 1000 s after switching on the NIR beam (time window A1). Arrows indicate the local in-plane displacement extracted from the speckle velocimetry analysis; the scale bar and the displacement-vector reference are shown in the figure.

the thermoelastic stresses generated in this way are extremely small. Previous short-time thermal-lens measurements on 9 wt% Mebiol yield, around 30 °C, a volumetric thermal expansivity of order $\alpha_V \simeq 2 \times 10^{-4}$ K^{-1} [40]. Importantly, this value was obtained from the early time thermal response, before the slower structural evolution of the gel becomes appreciable, and therefore characterizes the direct thermal expansion relevant to the initial thermoelastic forcing. Assuming isotropic expansion, the corresponding linear expansivity is $\alpha_L \simeq \alpha_V/3 \simeq 7 \times 10^{-5}$ K^{-1}. For the local temperature increase of approximately $\Delta T \simeq 3$ °C estimated here, this corresponds to a free thermal strain of order $\epsilon_{\rm th} \sim \alpha_L \Delta T \simeq 2 \times 10^{-4}$. A direct Young modulus for our 9 wt% Mebiol sample at this temperature is not available. Rheological data provided by the manufacturer for a closely comparable 10 wt% aqueous Mebiol sample give a storage modulus of a few 10^2 Pa around 30 °C. Taking $E \simeq 3G'$ as an order-of-magnitude estimate for a nearly incompressible gel therefore gives $E \sim 10^3$ Pa. A simple constrained-thermoelastic estimate then yields

$$\sigma_{\rm th} \sim E\alpha_L \Delta T \sim 10^{-1}\ \text{Pa}. \tag{15}$$

This value should be regarded as a characteristic fully constrained thermoelastic stress scale rather than as a direct measurement of the spatial stress field, since the actual sample geometry is only partially constrained and the gel can subsequently undergo viscoelastic, poroelastic, and structural relaxation.

In other words, the imposed thermal gradient generates a stress field that locally deforms the material and accelerates the dynamics compared with the case of a spatially uniform temperature. If the material were perfectly elastic, removal of the thermal field would restore the initial (unperturbed) state. Mebiol, however, is a *physical* gel: Its junctions are reversible and can rearrange, and the local polymer concentration can adjust in response to stress. Consequently, once the thermal gradient is removed the system may quickly return to thermal equilibrium, but it is no longer in mechanical equilibrium. Part of the stress remains "imprinted" in the sample, and the gel subsequently evolves slowly toward a new mechanical equilibrium. The relaxation of this residual stress drives additional microscopic rearrangements, thereby speeding-up the dynamics relative to an unperturbed sample held at the same temperature. To support this interpretation, we exploit the capability of PCI to quantify local deformations. Figure 6 shows the cumulative displacement field within the LR during the A1 time window, obtained using PIVlab [41]. The displacement

vectors indicate a net motion toward the region surrounding the IR-beam axis; additionally, the material appears to expand from the hotter side of the field of view (left side of the images) toward the colder side. Over 1000 s, the maximum displacement within the LR is on the order of 10 μm.

After switching off the IR beam, the speckle pattern decorrelates rapidly and the cross-correlation peak used by speckle velocimetry becomes less well defined. As a result, the spatial correlation analysis does not provide sufficiently reliable displacement estimates in this regime. We anticipate that employing a thinner cell and/or operating at a higher average temperature—thereby slowing down the intrinsic (unperturbed) dynamics—would improve the accuracy of the displacement-field reconstruction also after the IR laser is turned-off. The persistence of the deformation, measured both via PCI and thermal lens, suggests that, beyond reversible thermoelastic/poroelastic deformation, the network topology itself evolves during the excitation. This highlights a key difference between *chemical* gels (permanent crosslinks, fixed topology) and *physical* gels such as Mebiol (reversible junctions, evolving connectivity). For a chemical gel, once transient poroelastic equilibration is complete, unloading the thermal field is expected to restore the initial configuration (up to damage/fracture), because the topology is frozen and the deformation is stored elastically. In contrast, physical gels are transient networks: Crosslinks continuously dissociate and reassociate, implying stress relaxation and network remodeling on a characteristic restructuring time τ_r set by the junction lifetime and connectivity [42–44]. This picture suggests a timescale-controlled crossover governed by a Deborah-like ratio $\mathrm{De} \equiv \tau_r/t_{\mathrm{exc}}$, where t_{exc} is the duration of the thermal forcing. In the limit $t_{\mathrm{exc}} \ll \tau_r$ ($\mathrm{De} \gg 1$), the network topology is expected to remain effectively frozen during the excitation, favoring a predominantly quasielastic and reversible response. Conversely, for $t_{\mathrm{exc}} \gg \tau_r$ ($\mathrm{De} \ll 1$), bond exchange, solvent redistribution, and network remodeling can occur during the forcing, allowing persistent deformation to develop, as observed here. The present experiments probe the latter, long-duration regime and do not directly test the quasielastic limit. Accessing that regime would require a controlled pulsed-excitation protocol in which the forcing duration is short compared with the restructuring time while remaining sufficiently long to establish a measurable thermal perturbation. Such measurements would provide a direct test of the predicted crossover and are an interesting direction for future work.

In the next section, we consider a colloidal gel with physical bonds that are effectively permanent on the experimental timescale and whose mechanical and rheological properties are essentially temperature independent.

B. Polystyrene gel: an ultraweak colloidal gel and the role of convection

The PS gel discussed in this section is an ultraweak gel whose properties are essentially temperature independent [45]. The network is formed by salt-screened attractive interactions between the polystyrene particles. The bonds are therefore physical rather than chemical, but are effectively permanent on the timescale of the present experiments. The network is so fragile that even a small density mismatch of 0.001 g/cm^3 is sufficient to induce a measurable compression under the gel's own weight—despite the extremely low polymer concentration. Likewise, the shear generated when removing the cell from the holder can irreversibly damage the fractal gel structure. Nevertheless, although very weak, the gel still markedly suppresses solvent convection when the sample is illuminated by the infrared laser. Because forward scattering from this gel is not negligible, the transmitted-beam profile is noisy, and a quantitative TL analysis as accurate as that performed for Mebiol cannot be carried out. Even so, a clear perturbation of the beam propagation associated with the TL effect is still observable. Aside from an initial broadening of the transmitted beam occurring within the first few seconds of IR irradiation, the system rapidly reaches a stationary regime, with no evidence of strong convection. The fact that convection, if present, is extremely slow is supported by the observation that the gel does not break during IR exposure. Although the sample is 99.97% water, the tenuous fractal network is sufficient to strongly inhibit buoyancy-driven flow. A comparison of the microscopic dynamics through the field correlation function g_1 measured before and during IR irradiation does not reveal any significant change, consistent with a material whose intrinsic properties do not depend on temperature. However, inspection of the correlation index shows that the IR beam induces a weak but detectable perturbation: Shortly after the irradiation is started, and again a few seconds after the laser is switched off, small drops of the correlation index are observed. A visual inspection of the PCI images suggests that laser irradiation induces a clockwise rotation of the sample, followed by an opposite (counterclockwise) motion once the laser is switched off. To quantify this behavior, we measured the displacement field using the same speckle velocimetry procedure adopted for the Mebiol sample. The results, obtained at a laser drive current of 600 mA, are shown in Fig. 7. The displacement pattern closely resembles a convective roll. When the IR beam is turned on, the temperature gradient established in the sample generates

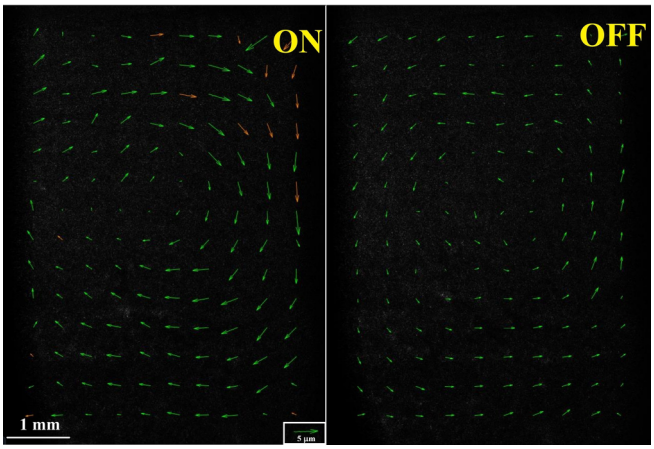


FIG. 7. Velocity field measured in a polystyrene gel ($\phi \simeq 3 \times 10^{-4}$, 16 mM $CaCl_2$) 10 s after switching on the NIR heating beam (left) and 10 s after switching the beam off (right). Arrows indicate the local in-plane velocity extracted from the speckle velocimetry analysis.

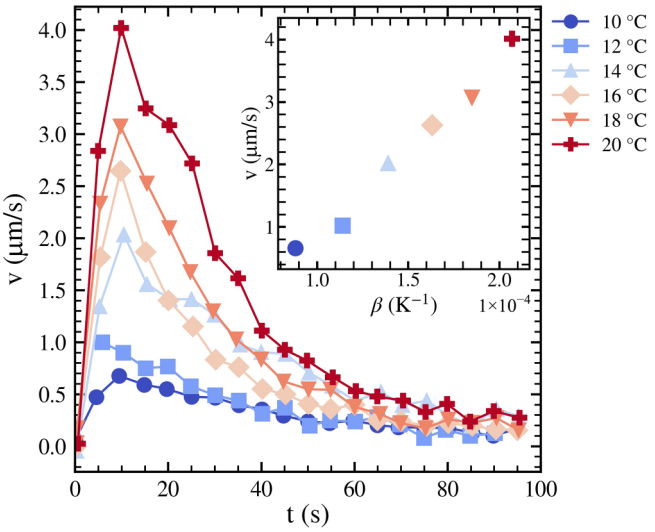


FIG. 8. Time evolution of the magnitude of the mean displacement velocity v in a polystyrene gel ($\phi \simeq 3 \times 10^{-4}$, 16 mM $CaCl_2$) for different sample temperatures, indicated in the legend. Inset: Maximum mean velocity v measured upon switching on the NIR beam at the highest power, for different initial sample temperatures. The maximum v is plotted as a function of the thermal expansivity β.

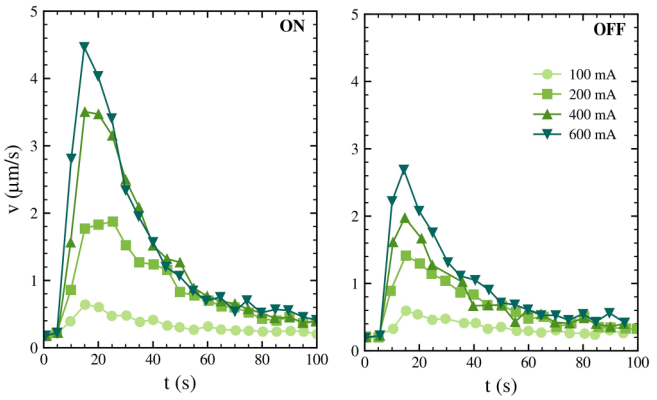


FIG. 9. Time evolution of the magnitude of the mean displacement velocity, v, in a polystyrene gel ($\phi \simeq 3 \times 10^{-4}$, 16 mM $CaCl_2$) for different NIR-laser powers (driving currents as indicated in the legend). Left: Response following laser switch on. Right: Recovery dynamics following laser switch off.

a buoyancy-driven flow. Because the left side of the cell is slightly hotter than the right side (the IR beam enters from the left), the solvent rises on the left side of the field of view, giving rise to a clockwise circulation. The resulting solvent motion deforms the gel network until the elastic restoring forces of the strands balance the viscous drag; at this point, the gel motion arrests and the displacement field reaches a plateau. After switching off the laser, the convective forcing vanishes and the system tends to recover its unperturbed configuration. During this recovery stage, the observed rotation is counterclockwise. A definitive confirmation that the observed deformation is convection driven is obtained by repeating the experiment at different initial sample temperatures. As is well known, the volumetric thermal expansion coefficient of water,

$$\beta = -\frac{1}{\rho}\left(\frac{\partial \rho}{\partial T}\right)_p,$$

is strongly temperature dependent and vanishes at the temperature of maximum density, $T \simeq 4$ °C. Within the Boussinesq approximation, the buoyancy force that sets the strength of natural convection is proportional to β. To compare the flow fields at different temperatures, we computed, for each frame, the spatial average of the velocity magnitude and we plot this quantity as a function of time in Fig. 8: An increase of T produces larger deformations. The inset of the figure reports the maximum average velocity measured in the sample at the highest pump power for different initial temperatures, together with the corresponding values of β for water, calculated using the Tilton and Taylor equation for water density [46]. In the explored interval (10 °C $< T <$ 20 °C), the maximum velocity grows approximately linearly with β, providing strong evidence that the sample deformation originates from buoyancy-driven convection. We repeated the experiment for different laser powers. As done for measurements at different temperatures, we plot the spatial average of the velocity field as a function of time in Fig. 9 for the four pump intensities investigated. The data indicate that, largely independent of laser power, the velocity reaches a maximum after approximately 10 s and then decays approximately exponentially to zero. As expected, increasing the pump power produces larger deformations: The resulting temperature gradient is steeper, which strengthens buoyancy-driven flow and leads to a faster convective roll. A notable feature emerges at low pump power: For the weakest irradiation, the displacement accumulated during the "laser on" phase is comparable to that recovered after switching off, indicating a predominantly elastic response and a near-complete return to the initial state. In contrast, at higher powers the displacement during irradiation is roughly twice that recovered during relaxation, suggesting that part of the deformation is irreversible, i.e., the gel undergoes plastic rearrangements. In an ultraweak gel, localized photothermal forcing offers a route to access a regime of ultralow stresses: The resulting viscous drag provides an extremely small and spatially distributed mechanical forcing that is difficult to impose with conventional rheometers without damaging or detaching the network at the boundaries. The observed power dependence, with a near-complete recovery at low powers and a partial irreversibility at higher powers, suggests that even such gentle forcing can cross from an elastic response to activated plastic rearrangements in the tenuous network. These observations motivate future experiments under pulsed excitation. In the purely elastic regime, the microscopic dynamics of the driven sample is expected to remain similar to that of an unperturbed gel. Conversely, if plastic events are activated, repeated pulsing may accelerate aging by promoting irreversible restructuring.

IV. DISCUSSION AND CONCLUSIONS

Our all-optical "stress-and-probe" protocol combines localized photothermal forcing with space-resolved dynamic light scattering. Thermal-lens (photothermal) techniques have a long history in *transparent* solid-state optics and material

characterization (e.g., laser glasses, thermo-optic coefficients, thermal transport) [35,36,47]; here, we repurpose thermal lensing in a soft, mechanically arrested medium and show that it can be tracked concomitantly with $\mathbf{u}(\mathbf{r}, t)$ and $c_I(\tau; \mathbf{r}, t)$ to reveal both transient heating and its possible persistence after the excitation. For the thermoreversible Mebiol gel, continuous NIR heating produces a pronounced, slowly evolving thermal-lensing signal and, more strikingly, a *persistent* lensing contribution that does not vanish after the pump is switched off. PCI reveals a concomitant acceleration of the microscopic dynamics in the heated region and an incomplete recovery after relaxation, pointing to an irreversible restructuring.

The polystyrene colloidal gel provides a complementary limit: Its intrinsic mechanical properties are approximately temperature independent, while the network is so fragile that even minute body forces (e.g., from density mismatch) can measurably load it. Under NIR heating, the displacement and velocity fields reconstructed from speckle velocimetry are consistent with a convective roll, identifying buoyancy-driven flow as the dominant source of stress in our geometry. In the case of porous materials as the ones investigated in this work, thermally driven interfacial transport (thermo-osmosis) could provide an additional, more subtle route by which ∇T can generate effective body forces and pressure gradients, potentially driving deformation even without buoyancy [48,49]. However, in terrestrial conditions these effects can be masked by gravity-induced convection, which is often practically unavoidable in optical heating geometries [30]. This motivates experiments under microgravity, where buoyancy is suppressed and transport induced by ∇T can be isolated. In this context, the COLIS facility onboard the International Space Station provides a unique platform to combine space-resolved light scattering with controlled NIR heating [50].

Looking forward, three directions appear particularly promising. First, for Mebiol it will be crucial to map the response as a function of the mean temperature, because both mechanical properties and junction lifetimes are strongly temperature dependent; at sufficiently high temperature, the spontaneous restructuring time may become so long that the material approaches the "chemical-gel" limit of a frozen topology. Second, geometry and boundary conditions (cell thickness, thermal anchoring, free versus constrained interfaces) should be treated as control parameters, since they reshape temperature, flow, and stress fields and can qualitatively change $\mathbf{u}(\mathbf{r}, t)$ and the spatial distribution of activity. Third, *pulsed* NIR excitation opens a route to study fatigue and damage accumulation in arrested soft solids using space-resolved dynamics: Soft materials provide intrinsically large time and length scales, making it feasible to directly visualize where and how irreversible events accumulate over cycles, a task that is far more challenging in conventional hard solids [51]. For instance, ground tests reported for COLIS already show that periodic NIR heating can *accelerate* the microscopic dynamics of a thermosensitive colloidal glass, and that repeated ON-OFF cycles lead to an accumulation of irreversible rearrangements reminiscent of cyclic shear protocols [50]. This strongly supports the idea that impulsive photothermal excitation can be used as a controlled route to investigate cyclic damage and fatigue in arrested soft solids, complementing purely mechanical fatigue studies in colloidal gels [51,52].

ACKNOWLEDGMENTS

We wish to thank Vincenzo Ruzzi and Jianzhu Ju for preliminary measurements on Mebiol gels. The work was partly funded by the Italian Ministry of University and Research (PRIN Project No. 20222MCY75) and by the Italian Space Agency (ASI, Project No. 2023-20-U.0–NESTEX).

DATA AVAILABILITY

The data that support the findings of this article are not publicly available upon publication because it is not technically feasible and/or the cost of preparing, depositing, and hosting the data would be prohibitive within the terms of this research project. The data are available from the authors upon reasonable request.

APPENDIX: ADDITIONAL ANALYSIS OF THE THERMAL-LENS RESPONSE

1. Long-time amplification of the thermal-lens signal

Although the diffraction patterns were not acquired with the dynamic range required for a quantitative phase retrieval, their long-time evolution provides a useful semiquantitative measure of the strengthening of the thermal lens. To illustrate this point, we consider a fixed-shape approximation in which the accumulated optical phase is written as

$$\Delta\phi(r, t) = A(t) f(r), \tag{A1}$$

where $f(r)$ describes the spatial shape of the lens and $A(t)$ its time-dependent amplitude.

In the geometrical-optics limit, the local deflection angle is related to the transverse phase gradient according to

$$\theta(r, t) \simeq \frac{1}{k}\left|\frac{\partial \Delta\phi(r, t)}{\partial r}\right| = \frac{A(t)}{k}|f'(r)|. \tag{A2}$$

Thus, if the shape of the phase profile remains approximately unchanged, the maximum diffraction angle, and consequently the radius of the outermost ring at a fixed observation distance, scale approximately with $A(t)$.

Experimentally, the outer-ring radius increases from approximately 7 mm at the beginning of the long-time measurements to about 45 mm at long times, corresponding to an increase by a factor of approximately 6–7. Within the fixed-shape approximation, this therefore indicates a comparable increase of the characteristic phase-gradient amplitude. This estimate should be regarded as semiquantitative: Changes in the spatial width or shape of the refractive-index profile would also affect the ring radius. Nevertheless, the several-fold growth occurring long after the thermal-diffusion time provides an independent indication that the long-time lensing response cannot be identified with the establishment of the initial temperature profile alone.

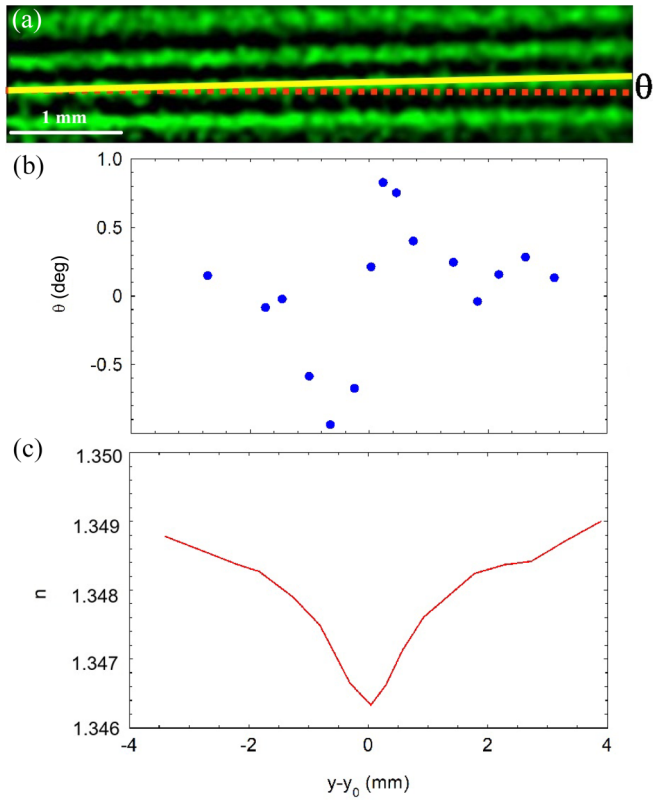


FIG. 10. (a) Image of the illumination stripes produced by residual inhomogeneities of the Powell-lens beam shaping for a 9 wt% Mebiol gel at $T = 30$ °C, 18 000 s after the beginning of NIR illumination. The red dashed line indicates the nominal propagation direction in the absence of a thermal lens, while the yellow solid line shows the deflected propagation direction in the presence of the thermal lens; θ is the angle between the two directions. Spatial scale bar is shown in the panel. (b) Deflection angle $\theta(y - y_0)$ as a function of the transverse coordinate, where y_0 denotes the symmetry axis of the NIR beam. (c) Effective refractive-index profile $n_{\text{eff}}(y - y_0)$ reconstructed from the measured deflection angles as described in the text.

2. Refractive-index reconstruction from illumination modulations

In the PCI setup, we employ a Powell lens. Although this element is designed to transform an incoming Gaussian beam into a nominally uniform (flattop) line, in practice the resulting intensity profile can exhibit residual modulations. These deviations from ideal uniformity mainly stem from the sensitivity of the Powell lens (owing to its aspheric design) to the spatial parameters of the incident beam (e.g., waist position, divergence, and alignment). As a consequence, the illumination at the sample is not perfectly homogeneous but displays weak intensity stripes parallel to the propagation direction. The amplitude of these modulations is typically limited (generally below ∼10%), yet it can be conveniently exploited to visualize ray paths within the TL. An example is shown in Fig. 10, where the stripe contrast is enhanced for clarity. While such intensity modulations represent a noise source for standard PCI correlation analysis and must be corrected, here we deliberately use them to infer the refractive-index profile.

In a homogeneous medium, the stripes remain parallel during propagation; when a TL develops in the sample, they bend in response to the local refractive-index gradient. In Fig. 10(a), the red dashed line indicates the reference propagation direction in the absence of TL effects, whereas the yellow solid line illustrates the deflected propagation path in the presence of the TL. We quantify this distortion by measuring, for each stripe, the deflection angle $\theta(y)$ as a function of its transverse position y, as reported in Fig. 10(b) for a gel sample 18 000 s after the beginning of the NIR illumination.

We then consider the sample as a weakly refracting gradient-index element of thickness L, whose refractive index may vary both in the transverse coordinate y and along the propagation direction z,

$$n = n(y, z). \tag{A3}$$

A collimated probe ray enters the sample at transverse position y_i with initial slope (paraxial angle) $\theta(0) = 0$, where

$$\theta(z) \equiv \frac{dy}{dz}. \tag{A4}$$

In the paraxial (small-angle) limit, the ray equation reduces to

$$\frac{d\theta}{dz} \simeq \frac{1}{n(y,z)} \frac{\partial n(y,z)}{\partial y}\bigg|_{y=y(z)} = \frac{\partial}{\partial y} \ln n(y,z)\bigg|_{y=y(z)}. \tag{A5}$$

If, as in our case, the total deflection is small enough that the ray does not drift significantly across the transverse gradient, one may approximate $y(z) \simeq y_i$ for $z \in [0, L]$. The output angle is then

$$\theta_{\text{out}}(y_i) \simeq \int_0^L \frac{\partial}{\partial y} \ln n(y_i, z)\, dz. \tag{A6}$$

It is convenient to define an effective path-averaged refractive-index profile $n_{\text{eff}}(y)$ through

$$\ln n_{\text{eff}}(y) \equiv \frac{1}{L} \int_0^L \ln n(y, z)\, dz. \tag{A7}$$

The previous equation can therefore be written as

$$\theta_{\text{out}}(y) \simeq L \frac{d}{dy} \ln n_{\text{eff}}(y). \tag{A8}$$

For the small refractive-index variations considered here, $n_{\text{eff}}(y)$ coincides, to first order, with the usual path-averaged refractive index. Rearranging the previous equation yields

$$\frac{d}{dy} \ln n_{\text{eff}}(y) \simeq \frac{\theta_{\text{out}}(y)}{L}. \tag{A9}$$

Integrating between a reference position y_{ref} and y gives

$$\ln n_{\text{eff}}(y) - \ln n_{\text{eff}}(y_{\text{ref}}) \simeq \frac{1}{L} \int_{y_{\text{ref}}}^{y} \theta_{\text{out}}(s)\, ds, \tag{A10}$$

and hence,

$$n_{\text{eff}}(y) \simeq n_{\text{eff}}(y_{\text{ref}}) \exp\left[\frac{1}{L} \int_{y_{\text{ref}}}^{y} \theta_{\text{out}}(s)\, ds\right]. \tag{A11}$$

If an absolute constraint is available, e.g., $n_{\text{eff}}(y) \to n_\infty$ as $|y| \to \infty$, one can eliminate the unknown constant by

choosing $y_{\mathrm{ref}} = \infty$:

$$n_{\mathrm{eff}}(y) \simeq n_\infty \exp\left[-\frac{1}{L}\int_y^\infty \theta_{\mathrm{out}}(s)\,ds\right]. \tag{A12}$$

In experiments with a finite data range, ∞ is replaced by the largest measured coordinate $y_{\max}$ for which $\theta_{\mathrm{out}}(y_{\max}) \simeq 0$ and $n_{\mathrm{eff}}(y_{\max}) \simeq n_\infty$.

In our analysis, we set $n_\infty = 1.348$, corresponding to the refractive index of 9 wt% Mebiol at approximately 30 °C obtained from previous refractometric characterization of the same system [40]. The reconstructed effective refractive-index profile is reported in Fig. 10(c). As expected for a diverging lens, $n_{\mathrm{eff}}(y)$ exhibits a minimum on the NIR-beam axis and increases toward its far-field value away from the irradiated region. If the observed index decrease were attributed entirely to the direct thermo-optic response, the corresponding temperature increase at the NIR-beam axis would need to exceed 20 °C. This is far larger than the approximately 3 °C thermal scale estimated from the initial scattered-intensity response, as discussed in the main text. As emphasized there, the latter value should be regarded as a semiquantitative estimate rather than as a direct temperature measurement. Nevertheless, the large discrepancy indicates that the long-time refractive-index modulation cannot be accounted for by the direct thermo-optic contribution alone, pointing to an additional contribution associated with the slow evolution of the gel.

[1] L. Berthier and G. Biroli, Theoretical perspective on the glass transition and amorphous materials, Rev. Mod. Phys. **83**, 587 (2011).

[2] Z. Filiberti, R. Piazza, and S. Buzzaccaro, Multiscale relaxation in aging colloidal gels: From localized plastic events to system-spanning quakes, Phys. Rev. E **100**, 042607 (2019).

[3] G. Brambilla, S. Buzzaccaro, R. Piazza, L. Berthier, and L. Cipelletti, Highly nonlinear dynamics in a slowly sedimenting colloidal gel, Phys. Rev. Lett. **106**, 118302 (2011).

[4] P. Schall, D. A. Weitz, and F. Spaepen, Structural rearrangements that govern flow in colloidal glasses, Science **318**, 1895 (2007).

[5] J. Colombo and E. Del Gado, Stress localization, stiffening, and yielding in a model colloidal gel, J. Rheol. **58**, 1089 (2014).

[6] S. Buzzaccaro, A. F. Mollame, and R. Piazza, Relaxation in aging thermoreversible gels: The role of thermal history, Soft Matter **17**, 7623 (2021).

[7] W. Nowacki, *Thermoelasticity*, 2nd ed. (Pergamon Press, Oxford, 1986).

[8] P. J. Chen, M. E. Gurtin, and W. O. Williams, On the thermodynamics of non-simple elastic materials with two temperatures, Z. Angew. Math. Phys. **20**, 107 (1969).

[9] H. M. Youssef, Theory of two-temperature-generalized thermoelasticity, IMA J. Appl. Math. **71**, 383 (2006).

[10] J. Alihemmati and Y. T. Beni, Generalized thermoelasticity of microstructures: Lord-Shulman theory with modified strain gradient theory, Mech. Mater. **172**, 104412 (2022).

[11] X. Wang and X. Xu, Thermoelastic wave in metal induced by ultrafast laser pulses, J. Therm. Stresses **25**, 457 (2002).

[12] C. B. Scruby, R. J. Dewhurst, D. A. Hutchins, and S. B. Palmer, Quantitative studies of thermally generated elastic waves in laser-irradiated metals, J. Appl. Phys. **51**, 6210 (1980).

[13] I. A. Veres, T. Berer, and P. Burgholzer, Numerical modeling of thermoelastic generation of ultrasound by laser irradiation in the coupled thermoelasticity, Ultrasonics **53**, 141 (2013).

[14] P. Vlugter, E. Block, and Y. Bellouard, Local tuning of fused silica thermal expansion coefficient using femtosecond laser, Phys. Rev. Mater. **3**, 053802 (2019).

[15] Q. Sun, T. Lee, M. Beresna, and G. Brambilla, Control of laser induced cumulative stress for efficient processing of fused silica, Sci. Rep. **10**, 3819 (2020).

[16] M. Sakakura, M. Terazima, Y. Shimotsuma, K. Miura, and K. Hirao, Thermal and shock induced modification inside a silica glass by focused femtosecond laser pulse, J. Appl. Phys. **109**, 023503 (2011).

[17] O. Koritsoglou, G. Duchateau, O. Uteza, and A. Mouskeftaras, Quantitative assessment of femtosecond laser-induced stress waves in fused silica, Phys. Rev. B **110**, 054112 (2024).

[18] M. A. Biot, General theory of three-dimensional consolidation, J. Appl. Phys. **12**, 155 (1941).

[19] D. F. McTigue, Thermoelastic response of fluid-saturated porous rock, J. Geophys. Res. **91**, 9533 (1986).

[20] T. Tanaka and D. J. Fillmore, Kinetics of swelling of gels, J. Chem. Phys. **70**, 1214 (1979).

[21] S. Cai and Z. Suo, Mechanics and chemical thermodynamics of phase transition in temperature-sensitive hydrogels, J. Mech. Phys. Solids **59**, 2259 (2011).

[22] A. Duri, D. A. Sessoms, V. Trappe, and L. Cipelletti, Resolving long-range spatial correlations in jammed colloidal systems using photon correlation imaging, Phys. Rev. Lett. **102**, 085702 (2009).

[23] R. Brighenti, M. P. Cosma, and N. Cohen, Mechanics and physics of the light-driven response of hydrogels, Mech. Res. Commun. **129**, 104077 (2023).

[24] J. Yoon, S. Cai, Z. Suo, and R. C. Hayward, Poroelastic swelling kinetics of thin hydrogel layers: Comparison of theory and experiment, Soft Matter **6**, 6004 (2010).

[25] J.-F. Louf and S. S. Datta, Poroelastic shape relaxation of hydrogel particles, Soft Matter **17**, 3840 (2021).

[26] S. Buzzaccaro, V. Ruzzi, T. Faleo, and R. Piazza, Microrheology of a thermosensitive gelling polymer for cell culture, J. Chem. Phys. **157**, 174901 (2022).

[27] R. Piazza, M. Campello, S. Buzzaccaro, and F. Sciortino, Phase behavior and microscopic dynamics of a thermosensitive gel-forming polymer, Macromolecules **54**, 3897 (2021).

[28] W. R. Callen, B. G. Huth, and R. H. Pantell, Optical patterns of thermally self-defocused light, Appl. Phys. Lett. **11**, 103 (1967).

[29] L. Deng, K. He, T. Zhou, and C. Li, Formation and evolution of far-field diffraction patterns of divergent and convergent Gaussian beams passing through self-focusing and self-defocusing media, J. Opt. A **7**, 409 (2005).

[30] R. Rusconi, L. Isa, and R. Piazza, Thermal-lensing measurement of particle thermophoresis in aqueous dispersions, J. Opt. Soc. Am. B **21**, 605 (2004).

[31] V. Ruzzi, S. Buzzaccaro, and R. Piazza, Thermal lens measurements of thermal expansivity in thermosensitive polymer solutions, Polymers **15**, 1283 (2023).

[32] Y. E. Geints, N. S. Panamarev, and A. A. Zemlyanov, Transient behavior of far-field diffraction patterns of a Gaussian laser beam due to the thermo-optical effect in metal nanocolloids, J. Opt. **13**, 055707 (2011).

[33] R. Karimzadeh, Spatial self-phase modulation of a laser beam propagating through liquids with self-induced natural convection flow, J. Opt. **14**, 095701 (2012).

[34] P. Zhang, M. Gandolfi, F. Banfi, C. Glorieux, and L. Liu, Time-resolved thermal lens investigation of glassy dynamics in supercooled liquids: Theory and experiments, J. Chem. Phys. **155**, 074503 (2021).

[35] C. Jacinto, D. N. Messias, A. A. Andrade, S. M. Lima, M. L. Baesso, and T. Catunda, Thermal lens and Z-scan measurements: Thermal and optical properties of laser glasses—A review, J. Non-Cryst. Solids **352**, 3582 (2006).

[36] K. Dobek, Thermal lensing: Outside of the lasing medium, Appl. Phys. B **128**, 18 (2022).

[37] J. Pátek, J. Hrubý, J. Klomfar, M. Součková, and A. H. Harvey, Reference correlations for thermophysical properties of liquid water at 0.1 MPa, J. Phys. Chem. Ref. Data **38**, 21 (2009).

[38] M. A. Biot, Thermoelasticity and irreversible thermodynamics, J. Appl. Phys. **27**, 240 (1956).

[39] B. A. Boley and J. H. Weiner, *Theory of Thermal Stresses* (Dover Publications, Mineola, NY, USA, 2012), reprint of the 1960 John Wiley & Sons ed.

[40] F. Rabino, Measurement of the thermal expansivity of thermoresponsive materials using an all-optical technique, Master's thesis, Politecnico di Milano, 2020.

[41] W. Thielicke and R. Sonntag, Particle image velocimetry for MATLAB: Accuracy and enhanced algorithms in PIVlab, J. Open Res. Software **9**, 12 (2021).

[42] M. S. Green and A. V. Tobolsky, A new approach to the theory of relaxing polymeric media, J. Chem. Phys. **14**, 80 (1946).

[43] A. S. Lodge, A network theory of flow birefringence and stress in concentrated polymer solutions, Trans. Faraday Soc. **52**, 120 (1956).

[44] G. A. Parada and X. Zhao, Ideal reversible polymer networks, Soft Matter **14**, 5186 (2018).

[45] S. Buzzaccaro, M. D. Alaimo, E. Secchi, and R. Piazza, Spatially-resolved heterogeneous dynamics in a strong colloidal gel, J. Phys.: Condens. Matter **27**, 194120 (2015).

[46] L. W. Tilton and J. K. Taylor, Accurate representation of the refractivity and density of distilled water as a function of temperature, J. Res. Natl. Bur. Stand. **18**, 205 (1937).

[47] L. C. M. Miranda, On the use of the thermal lens effect as a thermo-optical spectroscopy of solids, Appl. Phys. A **32**, 87 (1983).

[48] R. Piazza and A. Parola, Thermophoresis in colloidal suspensions, J. Phys.: Condens. Matter **20**, 153102 (2008).

[49] O. Farago, A simple statistical-mechanical interpretation of Onsager reciprocal relations and Derjaguin theory of thermo-osmosis, Eur. Phys. J. E **42**, 136 (2019).

[50] A. Martinelli, S. Buzzaccaro, Q. Galand, J. Behra, N. Segers, E. Leussink, Y. S. Dhillon, D. Maes, J. Lutsko, R. Piazza, and L. Cipelletti, An advanced light scattering apparatus for investigating soft matter onboard the International Space Station, npj Microgravity **10**, 115 (2024).

[51] J. M. van Doorn, J. E. Verweij, J. Sprakel, and J. van der Gucht, Strand plasticity governs fatigue in colloidal gels, Phys. Rev. Lett. **120**, 208005 (2018).

[52] J. E. Verweij, F. A. M. Leermakers, J. Sprakel, and J. van der Gucht, Plasticity in colloidal gel strands, Soft Matter **15**, 6447 (2019).